



Isotopic characterization of nitrogen oxides (NO_x), nitrous acid (HONO), and nitrate (NO₃⁻(p)) from laboratory biomass burning during FIREX

Jiajue Chai¹, David J. Miller^{1,a}, Eric Scheuer², Jack Dibb², Vanessa Selimovic³, Robert Yokelson³, Kyle J. Zarzana^{4,5,b}, Steven S. Brown^{4,6}, Abigail R. Koss^{4,5,6,c}, Carsten Warneke^{5,6}, Meredith Hastings¹

1. Department of Earth, Environmental and Planetary Sciences, and Institute at Brown for Environment and Society, Brown University, Providence, RI, USA
2. Institute for the Study of Earth, Ocean and Space, University of New Hampshire, Durham, NH, USA
3. Department of Chemistry, University of Montana, Missoula, USA
4. Chemical Sciences Division, NOAA Earth System Research Laboratory, Boulder, CO, USA
5. Cooperative Institute for Research in Environmental Sciences, University of Colorado, Boulder, CO, USA
6. Department of Chemistry, University of Colorado, Boulder, CO, USA
 - a. Now at: Environmental Defense Fund, Boston, MA, USA
 - b. Now at: Department of Chemistry, University of Colorado, Boulder, CO, USA
 - c. Department of Civil and Environmental Engineering, Massachusetts Institute of Technology, Cambridge, MA, USA

Correspondence: Jiajue Chai (jiajue_chai@brown.edu)



1 **Abstract**

2

3 New techniques have recently been developed to capture reactive nitrogen species for
4 accurate measurement of their isotopic composition. Reactive nitrogen species play
5 important roles in atmospheric oxidation capacity (hydroxyl radical and ozone formation)
6 and may have impacts on air quality and climate. Tracking reactive nitrogen species and
7 their chemistry in the atmosphere based upon concentration alone is challenging. Isotopic
8 analysis provides a potential tool for tracking the sources and chemistry of species such
9 as nitrogen oxides ($\text{NO}_x = \text{NO} + \text{NO}_2$), nitrous acid (HONO), nitric acid (HNO_3) and
10 particulate nitrate ($\text{NO}_3^-(p)$). Here we study direct biomass burning (BB) emissions
11 during the Fire Influence on Regional to Global Environments Experiment (FIREX, later
12 evolved into FIREX-AQ) laboratory experiments at the Missoula Fire Laboratory in the
13 fall of 2016.

14

15 An annular denuder system (ADS) developed to efficiently collect HONO for isotopic
16 composition analysis was deployed to the Fire Lab study. Concentrations of HONO
17 recovered from the ADS collection agree well with mean concentrations averaged over
18 each fire measured by 4 other high time resolution techniques, including mist
19 chamber/ion chromatography (MC/IC), open-path Fourier transform infrared
20 spectroscopy (OP-FTIR), cavity enhanced spectroscopy (CES), proton-transfer-reaction
21 time-of-flight mass spectrometer (PTR-ToF). The concentration validation ensures
22 complete collection of BB emitted HONO, of which the isotopic composition is
23 preserved during the collection process. In addition, the isotopic composition of NO_x and
24 $\text{NO}_3^-(p)$ from direct BB emissions were also characterized.

25 In 20 “stack” fires (direct emission within ~5 seconds of production by the fire) that
26 burned various biomass materials, $\delta^{15}\text{N}\text{-NO}_x$ ranges from -4.3 ‰ to +7.0 ‰, falling near
27 the middle of the range reported in previous work. The first measurements of $\delta^{15}\text{N}\text{-}$
28 HONO and $\delta^{18}\text{O}\text{-HONO}$ in biomass burning smoke reveal a range of -5.3 – +5.8 ‰ and
29 +5.2 – +15.2 ‰ respectively. Both HONO and NO_x are sourced from N in the biomass
30 fuel and $\delta^{15}\text{N}\text{-HONO}$ and $\delta^{15}\text{N}\text{-NO}_x$ are strongly correlated ($R^2 = 0.89$, $p < 0.001$),
31 suggesting NO_x and HONO are connected via formation pathways.

32

33 Our $\delta^{15}\text{N}$ of NO_x , HONO and $\text{NO}_3^-(p)$ ranges can serve as important biomass burning
34 source signatures, useful for constraining direct emissions of these species in
35 environmental applications. The $\delta^{18}\text{O}$ of HONO and NO_3^- obtained here verify our
36 method is capable of determining oxygen isotopic composition in BB plumes. The $\delta^{18}\text{O}$
37 for both species in this study reflect the laboratory conditions (i.e. a lack of
38 photochemistry), and would be expected to track with the influence of ozone (O_3),
39 photochemistry and nighttime chemistry in real environments. The methods used in this
40 study will be further applied in future field studies to quantitatively track reactive
41 nitrogen cycling in fresh and aged Western US wildfire plumes.

42

43

44

45

46



47 **1 Introduction**

48 Biomass burning (BB), which occurs in both anthropogenic processes (e.g. cooking,
49 heating, prescribed) and natural wildfire (lightning ignited vegetation burning), is a
50 significant source of atmospheric reactive nitrogen species, including nitrogen oxides
51 ($\text{NO}_x = \text{NO} + \text{NO}_2$), nitrous acid (HONO), nitric acid (HNO_3), particulate nitrate (NO_3^-
52 (p)), organic nitrates, peroxyacyl nitrate (PAN) and ammonia (NH_3) that have major
53 impacts on air quality and climate from regional to global scales (Crutzen and Andreae,
54 1990). Globally, biomass burning emits ~ 6 Tg of nitrogen oxides ($\text{NO}_x = \text{NO} + \text{NO}_2$) per
55 year, contributing at least 14% to total NO_x emissions (Jaeglé et al., 2005), with large
56 interannual and seasonal variation due to fire frequency and intensity (Jaffe and Briggs,
57 2012). Primarily emitted NO_x plays an important role in the photo-oxidation of volatile
58 and semi volatile organic compounds, which are present in high concentrations in BB
59 plumes, and strongly influences production of tropospheric ozone (O_3) and secondary
60 aerosols (Alvarado et al., 2015). In BB plumes, NO_x can be converted to PAN, which can
61 be transported long distances (100s to 1000s of km) in lofted plumes before rereleasing
62 NO_x . Therefore, BB emitted NO_x could widely influence air quality downwind for days
63 to weeks (Val Martín et al., 2006; Ye et al., 2016). In addition, NO_x is also the major
64 photochemical precursor of HNO_3 and NO_3^- (p), which can be transported downwind and
65 mixed with anthropogenic emissions impacting air quality and ecosystem health
66 (Hastings et al., 2013).

67 HONO has been observed in BB plumes in both laboratory and field experiments, with
68 HONO mixing ratios in the range of ~ 5 -33% of observed NO_x (Akagi et al., 2012, 2013;
69 Burling et al., 2010, 2011; Keene et al., 2006; Liu et al., 2016; Roberts et al., 2010;
70 Selimovic et al., 2018; Yokelson et al., 2007, 2009). Photolysis of HONO is a major OH
71 precursor in the daytime; therefore HONO plays an important role in photochemical
72 aging of BB plumes and atmospheric oxidation capacity at regional scales (Alvarado and
73 Prinn, 2009; Liu et al., 2016; Tkacik et al., 2017; Trentmann et al., 2005). HONO has
74 been proposed as a significant OH source in BB plumes and the inclusion of HONO in
75 photochemical models could explain much of the uncertainty in the modeled O_3
76 (Alvarado et al., 2009; Alvarado and Prinn, 2009; Cook et al., 2007; Travis et al., 2016;
77 Trentmann et al., 2005).

78 Direct BB emission factor measurements of HONO and NO_x exhibit significant
79 uncertainties due to limited observations and large spatial and temporal variability of
80 burning conditions, making it challenging to build an accurate inventory of BB emissions
81 relative to other major sources (Lapina et al., 2008). Emission factors vary and mainly
82 depend on 1) fuel nitrogen content (0.2 – 4% by mass), which is a function of vegetation
83 type, and 2) modified combustion efficiency ($\text{MCE} = \Delta[\text{CO}_2]/(\Delta[\text{DCO}] + \Delta[\text{CO}_2])$) that is
84 determined by combustion conditions including fuel moisture, fuel load, temperature,
85 relative humidity, wind speed, and other meteorological parameters (Burling et al., 2010;
86 Jaffe and Briggs, 2012; Yokelson et al., 1996). Additionally, the temporal evolution of
87 HONO in BB plumes varies greatly in different fires and relative contributions from
88 direct emission versus NO_2 conversion to HONO remains unclear. For instance,
89 significant concentrations of HONO and correlation between HONO and NO_2 have been
90 observed in aged plumes, indicating the importance of heterogeneous conversion of NO_2 -
91 to-HONO on BB aerosols (Nie et al., 2015). By contrast, no evidence was found for



92 secondary HONO formation in a BB plume during the Southeast Nexus Experiment
93 (Neuman et al., 2016). HONO directly emitted from BB is important in constraining
94 HONO formed during plume aging and the total HONO budget (reducing uncertainties)
95 and increasing our understanding of HONO impacts on O₃ and secondary aerosol
96 formation downwind of BB regions.

97
98 In an effort to better understand reactive nitrogen emissions and chemistry, especially for
99 HONO, new techniques have been developed to analyze the isotopic composition of
100 various species. Stable isotopes provide a unique approach of characterizing and tracking
101 various sources and chemistry for a species of interest (Hastings et al., 2013). Fibiger et
102 al. (2014) developed a method to quantitatively collect NO_x in solution as NO₃⁻ for
103 isotopic analysis, which has been verified to avoid any isotopic fractionation during
104 collection in both lab and field studies. This allows for high-resolution measurement of
105 δ¹⁵N-NO_x in minutes to hours depending on ambient NO_x concentrations ($\delta^{15}\text{N} =$
106 $[(^{15}\text{N}/^{14}\text{N})_{\text{sample}}/(^{15}\text{N}/^{14}\text{N})_{\text{air-N}_2} - 1] \times 1000\text{‰}$, and $\delta^{18}\text{O} = [(^{18}\text{O}/^{16}\text{O})_{\text{sample}}/(^{18}\text{O}/^{16}\text{O})_{\text{VSMOW}} -$
107 $1] \times 1000\text{‰}$ where VSMOW is Vienna Standard Mean Ocean Water). δ¹⁵N has also been
108 used to track gaseous NO_x from a variety of major sources including emissions from
109 biomass burning (Fibiger and Hastings, 2016), vehicles (Miller et al., 2017), and
110 agricultural soils (Miller et al., 2018). Using this method, Fibiger et al. (2016)
111 systematically investigated BB δ¹⁵N-NO_x from different types of biomass from around
112 the world in a controlled environment during the fourth Fire Lab at Missoula Experiment
113 (FLAME-4). NO_x emissions collected both immediately from the BB source and 1-2
114 hours after the burn in a closed environment ranged from -7 to +12‰, and primarily
115 depended on the δ¹⁵N of the biomass itself. BB emitted HONO isotopic composition has
116 never been measured before. Our recently developed method for HONO isotopic
117 composition analysis (Chai and Hastings, 2018) enables us to not only characterize δ¹⁵N
118 and δ¹⁸O of HONO, but also explore the connection between δ¹⁵N-NO_x and δ¹⁵N-HONO.

119
120 The Fire Influence on Regional to Global Environments Experiment and Air Quality
121 (FIREX-AQ) investigates the influence of fires in the western U.S. on climate and air
122 quality, via an intensive, multi-platform, campaign. The first phase of FIREX-AQ took
123 place at the US Forest Service Fire Sciences Laboratory (FSL) in Missoula, Montana, in
124 the fall of 2016, where we measured δ¹⁵N-NO_x, δ¹⁵N-HONO, δ¹⁸O-HONO, δ¹⁵N-NO₃⁻
125 (p), δ¹⁸O-NO₃⁻(p) and δ¹⁵N-biomass in 20 “stack burns” of a variety of fuels
126 representative of northwestern North America. Here we report on the results and explore
127 relationships between the isotopic composition of these nitrogen oxides, as well as the
128 corresponding mixing ratios for HONO that were concurrently measured by a variety of
129 techniques. This work offers characterization and quantification of BB source signatures
130 of these species, which can be applied in the interpretation of observations in future field
131 studies.

132
133
134
135
136
137



138 2. Experimental details

139 2.1 FIREX Fire Science Laboratory design

140

141 The room for controlled BB experiments is $12.5 \times 12.5 \text{ m} \times 22 \text{ m}$, with a continuously
142 weighed fuel bed at the center of the room. The combustion exhaust was vented at a
143 constant flow rate ($\sim 3.3 \text{ m s}^{-1}$) through a 3.6 m diameter inverted funnel followed by a
144 1.6 m diameter stack, and collected at a platform 17 m above the fuel bed via sampling
145 ports that surround the stack, resulting in a transport time of $\sim 5 \text{ s}$. Further details have
146 been described in the literature (Stockwell et al., 2014). All of our instruments for
147 sampling and online measurements were placed on the platform, which can accommodate
148 up to 1820 kg of equipment and operators. Measurements were focused on the “stack
149 burns”, for which fires lasted a few minutes up to 40 minutes.

150

151 For this study, we investigated 20 stack fires of vegetation types abundant in the western
152 US, representing coniferous ecosystems, including ponderosa pine (PIPO), lodgepole
153 pine (PICO), Engelmann spruce (PIEN), Douglas-fir (PSME) and subalpine fir (ABLA),
154 with replicate burns for most of these types (Table 1). Some of the fires proceeded by
155 burning of an individual fuel component such as litter, canopy, duff and rotten logs.
156 Other fires simulated actual biomass in the coniferous ecosystem by mixing various fuel
157 components in realistically recreated ecosystem matrices using the first order fire effects
158 model (FOFEM) (Reinhardt et al., 1997).

159

160

161 2.2 Instrumentation

162

163 2.2.1 Collection of HONO, NO_x and nitrate for isotopic analysis

164 HONO was completely collected for isotopic analysis using an annular denuder system
165 (ADS) (Chai and Hastings, 2018). The ADS system deployed in this laboratory
166 experiment consisted of a Teflon particulate filter, a Nylasorb filter to remove HNO₃,
167 followed by two annular denuders, each coated with a solution of 10 mL of Na₂CO₃ (1%
168 w/v) + glycerol (1% v/v) + methanol–H₂O solution (1:1 volume ratio) following a
169 standard EPA method. Methanol and glycerol are certified ACS plus with a purity of
170 $\geq 99.8\%$ and $\geq 99.5\%$, respectively. After coating, the denuders are dried using zero air
171 and capped immediately. Within 6 hours after each collection, the coating was extracted
172 in 10 mL of ultrapure water (18.2 M Ω) in two sequential 5 mL extractions. The extracted
173 solution with a pH of ~ 10 was transported to Brown University for concentration and
174 isotopic analysis 3–14 days after the sampling. The timescales for sample extraction and
175 isotopic analysis preserve both the solution concentration and isotopic composition of
176 HONO in the form of nitrite (Chai and Hastings, 2018). The two-denuder set up allows
177 us to minimize the interference for both concentration and isotopic analysis from other N-
178 containing species that could be trapped and form nitrite in residual amounts on the
179 denuders, especially NO₂. Our method development study showed NO₂ tends to absorb in
180 the same amount (difference $< 4\%$) on the walls of each denuder in a train setup, which is
181 consistent with other studies (Perrino et al., 1990; Zhou et al., 2018). On the basis of this
182 validation, the second denuder extract is used to correct the first denuder extract for both
183 concentration and isotopic composition (Chai and Hastings, 2018). Note HONO levels



184 were above the minimum detection limit (0.07 μM) and the breakthrough amount of
185 HONO threshold is far from being reached given the concentrations (Table 1), flow rate
186 (~ 4 L/min) and collection times (5 - 40 min). The necessary amount minimum of nitrite
187 collected for isotopic analysis is 10 - 20 nmol.

188
189 Following the ADS, to avoid scrubbing of HONO, are a flow meter (Omega) and the
190 NO_x collection system for analysis of $\delta^{15}\text{N}\text{-NO}_x$ (Fibiger et al., 2014; Fibiger and
191 Hastings, 2016; Wojtal et al., 2016). In brief, NO_x is collected in a solution containing
192 0.25 M KMnO_4 and 0.5 M NaOH which oxidizes NO and NO_2 to NO_3^- by pumping
193 sampled air through a gas washing bottle with a 65 Watts diaphragm vacuum pump. The
194 flow rate (~ 4 L/min with 1% uncertainty) is controlled with a critical orifice inserted
195 between the pump and gas stream outlet, and is monitored and recorded with a flow
196 meter placed prior to the NO_x collector. The NO_x trapping solution blanks are also
197 collected every day to quantify background NO_3^- for concentration and isotopic blank
198 corrections. The Omega flow meter was calibrated with another flow meter (Dry Cal Pro)
199 by varying flow rates. Within a day after collection, we stabilized the samples in the wet
200 chemistry lab in the Fire Science Lab by adding 30% w/w H_2O_2 that reduces MnO_4^- to
201 MnO_2 precipitate before being shipped back to Brown University for further processing.
202 This effectively excludes the possible interferences from NH_3 that could be oxidized to
203 NO_3^- by MnO_4^- after a week (Miller et al., 2017) and references therein). The samples
204 were neutralized with 12.1 N HCl in the Brown lab, before concentration measurement
205 and isotopic analyses. NO_3^- on the upstream Millipore filters and HNO_3 from the
206 Nylasorb filters, if there was any, were extracted by sonicating the filters in ~ 30 mL
207 ultrapure H_2O (18.2 $\text{M}\Omega$). Samples with $[\text{NO}_3^-] > 1$ μM were analyzed for isotopic
208 composition (concentration techniques detailed below).

209
210 All treated samples from both HONO collection and NO_x collection and their
211 corresponding blanks were analyzed offline for concentrations of NO_2^- and NO_3^- with a
212 WestCo SmartChem 200 Discrete Analyzer colorimetric system. The reproducibility of
213 the concentration measurement was ± 0.3 $\mu\text{mol L}^{-1}$ (1σ) for NO_2^- and ± 0.4 $\mu\text{mol L}^{-1}$ for
214 NO_3^- when a sample was repeatedly measured ($n = 30$). A detection limit of 0.07 μmol
215 L^{-1} for NO_2^- and 0.1 $\mu\text{mol L}^{-1}$ for NO_3^- was determined, and no detectable nitrite or
216 nitrate was found in the blank denuder coating solution, whereas blank NO_3^-
217 concentrations of ~ 5 μM are typical for the NO_x collection method (Fibiger et al., 2014;
218 Wojtal et al., 2016). Note that NO_3^- concentration was measured on the ADS solutions to
219 verify whether and to what extent NO_2^- was oxidized to NO_3^- on denuder walls because
220 the denitrifier method will convert both NO_3^- and NO_2^- to N_2O for isotopic analysis (see
221 below). In addition, samples collected with a mist chamber/ion chromatography system
222 (described in Sect. 2.2.2) were also tested for their concentrations and only those with
223 sufficient nitrite quantity were further analyzed for isotopic composition.

224

225 **2.2.2 NO_x and HONO online concentration measurement**

226 NO and NO_x concentrations were measured with a Thermo Scientific Model 42i
227 chemiluminescence NO/NO_x analyzer, with ± 0.4 ppbv precision and 0.2 ppbv zero noise
228 at 1 minute time resolution. In the NO channel, O_3 generated by an ozonator titrates NO
229 to excited state NO_2 which subsequently produces luminescence that is proportional to



230 NO concentration. In the NO_x channel, the sample gas stream first flows through a heated
231 molybdenum catalyst (325 °C) that converts NO₂ to NO before entering the NO+O₃
232 reaction chamber. The auto cycle mode (NO/NO_x) switches the mode solenoid valve
233 automatically on a 10 second cycle so that NO, NO₂, and NO_x concentrations are
234 determined. It is known that some NO_y species including HONO, HNO₃, organic nitrate
235 and PAN can be partially converted to NO in the hot molybdenum catalyst, causing
236 positive artifacts in measured NO_x (Reed et al., 2016). In this study, only the HONO
237 interference was corrected using our ADS measured HONO concentration; contributions
238 from HNO₃, PAN and gaseous organic nitrate are not of major concern because no photo-
239 oxidation is involved in indoor fires (Koss et al., 2018; Selimovic et al., 2018; Stockwell
240 et al., 2014). In addition, we do not expect that other reactive nitrogen species such as
241 NH₃ and hydrogen cyanide (HCN) interfere with NO₂ measurement. A particulate matter
242 filter (Millipore, 1µm PTFE) was always placed before the inlet of the NO_x analyzer. The
243 NO channel was calibrated before and after the entire Fire Lab experiments with standard
244 NO (10 ppmv in N₂) diluted with zero air (Thermo Fisher Scientific, Model 111) via a
245 gas dilution calibrator (Thermo Fisher Scientific, Model 146i) and NO₂ response of the
246 NO_x channel using O₃ titration is within ±5% accuracy. The NO_x measurement verified
247 the concentration of the NO_x collected for isotopic analysis, and the original NO_x data is
248 available in the NOAA FIREX archive (FIREX, 2016).

249 HONO and HNO₃ concentrations were measured using the University of New
250 Hampshire's dual mist chamber/ion chromatograph system (Scheuer et al., 2003) with the
251 sampling inlet placed right next to that of the ADS. The dual channel IC system is custom
252 built using primarily Dionex analytical components. Briefly, automated syringe pumps
253 are used to move samples and standard solutions in a closed system, which minimizes
254 potential contamination. A concentrator column and 5 ml injections were used to improve
255 sensitivity. Eluents are purged and maintained under a pressurized helium atmosphere.
256 Background signal is minimized using electronic suppression (Dionex-ASRS). The
257 chromatography columns and detectors are maintained at 40 °C to minimize baseline
258 drifting. A tri-fluoro-acetate tracer spike into the ultra-clean sampling water is used as an
259 internal tracer of sample solution volume, which can decrease due to evaporation in the
260 exhaust flow by 10-20% depending on the ambient conditions and length of the sample
261 integration interval. In this work, each sample integrated 5 minutes of collection. The
262 spike was analyzed to correct the final mist chamber sampled solution volume with an
263 uncertainty of ±3%. This system has been deployed to various field studies for HONO
264 measurement (Dibb et al., 2002; Stutz et al., 2010) and showed reasonable
265 intercomparison with other HONO measurement techniques (within 16% uncertainty)
266 during the 2009 SHARP campaign in Houston (Pinto et al., 2014). The detection limits
267 for HNO₃ and HONO are 10 ppt for 5-minute sample integrations. During the
268 experiments, two mist chambers were operated to collect gas samples in parallel, each
269 with an integration interval of 5 min. One channel of the IC was utilized for concentration
270 measurement; in the other, the mist chamber's solution was transferred into a sample
271 bottle using the syringe pump, and the collected solution was brought to Brown
272 University for isotopic analysis of HNO₃ if sufficient amount (10-20 nmol) was collected
273 for each sample.

274
275 In addition to MC/IC, the HONO mixing ratios were also measured using high time-



276 resolution (~1 second) measurement techniques including open-path Fourier transform
277 infrared spectroscopy (OP-FTIR) (Selimovic et al., 2018), cavity enhanced spectrometer
278 (CES) (Min et al., 2016; Zarzana et al., 2018), and proton-transfer-reaction time-of-flight
279 mass spectrometer (PTR-ToF). Inlet ports of CES and PTR-ToF were placed 5' apart
280 from, but at the same height on the platform as those for ADS and MC/IC, while the OP-
281 FTIR had an open path cell at the stack. The smoke has been shown to be well-mixed at
282 the sampling platform (Christian et al., 2004) and the mean HONO mixing ratios across
283 each fire obtained from the four techniques were compared with that retrieved from ADS
284 collection. This offers comprehensive verification of complete capture of HONO by ADS
285 that is extremely important for conserving the isotopic composition of HONO.

286 The details of OP-FTIR are described in previous works (Selimovic et al., 2018;
287 Stockwell et al., 2014). The setup included a Bruker MATRIX-M IR cube spectrometer
288 with a mercury cadmium telluride (MCT) liquid-nitrogen-cooled detector interfaced with
289 a 1.6 m base open-path White cell. The white cell was positioned on the platform and its
290 open path spanned the width of the stack. This facilitates direct measurement across the
291 rising emissions. The optical path length was set to 58 m. The IR spectra resolution was
292 0.67 cm^{-1} from $600\text{--}4000\text{ cm}^{-1}$. Pressure and temperature were continuously recorded
293 with a pressure transducer and two temperature sensors respectively, which were placed
294 adjacent to the White cell optical path. They were used for spectral analysis. Time
295 resolution for stack burns was approximately 1.37 s. The OP-FTIR measures CO_2 , CO ,
296 CH_4 , a series of volatile organic compounds and various reactive nitrogen species
297 (Selimovic et al., 2018).—Mixing ratios of HONO were retrieved via multicomponent
298 fitting to a section of the mid-IR transmission spectra with a synthetic calibration
299 nonlinear least-squares method (Griffith, 1996; Yokelson et al., 2007), and both the
300 HITRAN spectral database and reference spectra recorded at the Pacific Northwest
301 National Laboratory (Rothman et al., 2009; Sharpe et al., 2004; Johnson et al., 2010,
302 2013) were used for the fitting. The uncertainty is ~10% for the HONO mixing ratio
303 measurement and the detection limit is no more than a few ppb as reported in previous
304 studies (Stockwell et al., 2014; Veres et al., 2010).

305 Nitrous acid measurements by cavity enhanced spectroscopy used the airborne cavity
306 enhanced spectrometer, ACES, recently described by Min *et al.* (2016). This instrument
307 consists of two channels, one measuring over the spectral range from 438–468 nm where
308 glyoxal (CHOCHO) and NO_2 have structured absorption bands, and one measuring over
309 from 361–389 nm, where HONO has structured absorption. In the HONO channel, light
310 from an LED centered at 368 nm and with an output power of 450 mW and collimated
311 with an off-axis parabolic collector illuminates the input mirror of a 48 cm optical cavity
312 formed from mirrors with a maximum reflectivity $R = 99.98\%$ at 375 nm. The effective
313 path length within the optical cavity is $> 3\text{ km}$ over the region of greatest reflectivity. The
314 mirror reflectivity (effective path length) was calibrated from the difference in Rayleigh
315 scattering between He and zero air to provide an absolute calibration of the instrument
316 response. A fiber optic bundle collects light exiting the optical cavity and transmits it to
317 a grating spectrometer with a CCD detector, where it is spectrally dispersed at a
318 resolution of 0.8 nm. The resulting spectra are fit using DOASIS software (Kraus, 2006)
319 to determine trace gas concentrations, including NO_2 , HONO and O_4 . Mixing ratios of
320 NO_2 and HONO are reported at 1 s resolution, although the NO_2 precision is higher in the



321 455 nm channel. The 1 Hz HONO precision is 800 pptv (2σ). (The precision of the
322 HONO instrument in ACES is somewhat degraded by the optimization of 455 nm
323 channel for glyoxal detection, which reduces the photon count rate on the 368 nm
324 channel.) The accuracy of the HONO measurement is 9%. Air was sampled directly
325 from stack at a height of 15 m above the fuel bed through a 1 m length of ¼" O.D. Teflon
326 (FEP) tubing as described in Zarzana *et al.* (2018). The residence time in the inlet and
327 sample cells was < 1 s. Comparison between the ACES HONO and an open path FTIR
328 agreed to within 13% on average, and ACES HONO was well correlated with 1Hz
329 measurements from a PTR-ToF ($r^2 = 0.95$) (Koss *et al.*, 2018).

330 The PTR-ToF instrument used in the FIREX Fire Lab experiment is described in detail in
331 previous studies (Koss *et al.*, 2018; Yuan *et al.*, 2016). The PTR-ToF instrument is a
332 chemical ionization mass spectrometer typically using H_3O^+ reagent ions and a wide range
333 of trace gases can be detected in the range of tens to hundreds of parts per trillion (pptv)
334 for a 1 s measurement time. At the Fire Lab, PTR-ToF detected several inorganic species
335 including HONO with an uncertainty of 15%. HONO is detected at a lower sensitivity
336 than most trace gases in PTR-ToF, but mixing ratios for all fires were well above the
337 detection limit.

338

339 2.2.3 Isotopic composition measurements

340 The denitrifier method was used to complete nitrogen and oxygen isotope analyses
341 ($^{15}\text{N}/^{14}\text{N}$, $^{18}\text{O}/^{16}\text{O}$) of NO_3^- and/or NO_2^- , by quantitative conversion to N_2O by
342 denitrifying bacteria *P. aureofaciens* (Casciotti *et al.*, 2002; Sigman *et al.*, 2001). The
343 isotopic composition of N_2O is then determined by a Thermo Finnegan Delta V Plus
344 isotope ratio mass spectrometer at m/z 44, 45 and 46 for $^{14}\text{N}^{14}\text{N}^{16}\text{O}$, $^{14}\text{N}^{15}\text{N}^{16}\text{O}$ and
345 $^{14}\text{N}^{14}\text{N}^{18}\text{O}$, respectively. Sample analyses were corrected against replicate measurements
346 of the NO_3^- isotopic reference materials USGS34, USGS35, and IAEA-NO-3 (Böhlke
347 *et al.*, 2003). Precisions for $\delta^{15}\text{N}$ -HONO and $\delta^{15}\text{N}$ - NO_x isotopic analysis across each of the
348 entire methods are $\pm 0.5\%$ and $\pm 1.3\%$, respectively (Chai and Hastings, 2018; Fibiger
349 *et al.*, 2014). $\delta^{18}\text{O}$ - N_2O from the NO_x collection samples was measured but is not reported
350 as $\delta^{18}\text{O}$ - NO_x because it is greatly impacted by MnO_4^- oxidation and does not represent
351 the $\delta^{18}\text{O}$ - NO_x in the sample air. The total $\delta^{15}\text{N}$ of the starting biomass ($\delta^{15}\text{N}$ -biomass)
352 was measured at the Marine Biological Laboratory Ecosystems Center Stable Isotope
353 Facility. The materials measured for $\delta^{15}\text{N}$ -biomass (Table S1) cover most but not all the
354 biomass types burned in the experiments depending on availability of the leftover
355 materials. Analyses were conducted using a Europa ANCA-SL elemental analyzer–gas
356 chromatograph preparation system interfaced with a Europa 20–20 continuous-flow gas
357 source stable isotope ratio mass spectrometer. Analytical precision was $\pm 0.1\%$, based on
358 replicate analyses of international reference materials.

359 Collection time spanned the whole fire burning (5 min to 40 min) in order to maximize
360 the signal. We chose to report the samples whose concentrations are at least 30% above
361 the $5 \mu\text{M}$ NO_3^- present in the blank KMnO_4 solution upon purchase (Fibiger *et al.*, 2014),
362 such that the propagated error through the blank correction does not exceed the analytical
363 precision of $\pm 1.5\%$ for $\delta^{15}\text{N}$ - NO_x . We found identical concentration and isotopic
364 signatures for both field and laboratory blanks, which ensures that no additional NO_3^-



365 contamination was introduced into the KMnO_4 solutions in the gas-washing bottle. In
366 addition, fires with high particulate loading that resulted in $>50\%$ reduction in flow rate
367 are not considered for isotopic analysis because the low flow rate could induce
368 incomplete collection with potential isotopic fractionation that might not represent BB
369 emissions.

370

371 **3. Results and discussion**

372

373 **3.1 Temporal evolution of HONO and HNO_3 from direct BB emissions**

374

375 The time series of HONO and HNO_3 concentrations measured by MC/IC at 5-minute
376 resolution for each available stack fire are shown in Fig. 1, and original data can be found
377 in the NOAA data archive (FIREX, 2016). HNO_3 concentrations were nearly two orders
378 of magnitude lower than typical HONO concentrations. The constant low concentration
379 of HNO_3 from fresh emissions across all fires is consistent with the findings in (Keene et
380 al., 2006), confirming HNO_3 is not a primary reactive nitrogen species in fresh smoke.
381 Rather, it is largely produced secondarily in aged smoke and nighttime chemistry. Both
382 HONO and HNO_3 mixing ratios reach their peak in the first five minutes, except for fire
383 no. 12 (Engelmann spruce - duff), from which HONO concentration remains nearly
384 constant over the course of each fire, but much lower than HONO concentration of the
385 rest of the fires. The largest HONO and HNO_3 were emitted from burning subalpine fir-
386 Fish Lake canopy (fire no. 15), integrated concentration of up to 177 ppbv and 1.9 ppbv
387 in the first 5-minute sample, respectively. We note that fires no. 12 has the smallest MCE
388 value 0.868 (FIREX, 2016). In general, the closer the MCE value is to 1, the more likely
389 N-oxidation (e.g. NO_x and HONO) dominates over N-reduction (e.g. NH_3 and HCN) as a
390 result of flaming; when MCE approaches 0.8, more smoldering occurs such that N-
391 reduction becomes dominant (Ferek et al., 1998; Goode et al., 1999; McMeeking et al.,
392 2009; Yokelson et al., 1996, 2008). Accordingly, the smoldering combustion condition of
393 fire no. 12 leads to lower concentration of oxidized nitrogen species than the rest of the
394 fires in this study. In addition, HONO/ NO_x ratio ranged from 0.13 to 0.53 with a mean of
395 0.29 ± 0.12 , comparable with previous results of laboratory experiments (0.11 ± 0.04) and
396 field experiments (0.23 ± 0.09) (Akagi et al., 2013; Burling et al., 2010, 2011)

397

398 **3.2 Verification of ADS collected HONO concentration**

399 The HONO collected with the ADS represents a mean value over the course of each
400 entire burn. We first compare HONO concentration recovered from the ADS, denoted as
401 $[\text{HONO}]_{\text{ADS}}$, with that measured with the collocated MC/IC when both measurements
402 were available (Fig. 2). The comparison demonstrates good consistency across all fires,
403 with the $[\text{HONO}]_{\text{ADS}}$ of all available fires falling within the first and third quartile of
404 MC/IC HONO data. Additionally, we made intercomparisons between $[\text{HONO}]_{\text{ADS}}$ with
405 mean values of various high resolution methods including MC/IC, OP-FTIR, ACES and
406 PTR-ToF that are also available from the NOAA data archive (Fig. 3; FIREX, 2016). The
407 mean values used for the comparison are shown in Table S2. The linear regression results
408 for all four comparisons are:

409

$$410 \quad [\text{HONO}]_{\text{ADS}} = (1.07 \pm 0.24) [\text{HONO}]_{\text{MCIC}} - 0.72 \quad \text{Eq. (1)}$$



411 $(R^2 = 0.63; p_{\text{slope}} < 0.001, p_{\text{intercept}}=0.95);$
412
413 $[\text{HONO}]_{\text{ADS}} = (1.07 \pm 0.08) [\text{HONO}]_{\text{ACES}} - 4.63$ Eq. (2)
414 $(R^2 = 0.95; p_{\text{slope}} < 1 \times 10^{-6}, p_{\text{intercept}}=0.32);$
415

416 $[\text{HONO}]_{\text{ADS}} = (1.07 \pm 0.22) [\text{HONO}]_{\text{FTIR}} + 5.48$ Eq. (3)
417 $(R^2 = 0.75; p_{\text{slope}} < 0.005, p_{\text{intercept}}=0.48);$
418

419 $[\text{HONO}]_{\text{ADS}} = (1.08 \pm 0.19) [\text{HONO}]_{\text{PTR-ToF}} - 8.81$ Eq. (4)
420 $(R^2 = 0.87; p_{\text{slope}} < 0.005, p_{\text{intercept}}=0.28).$
421

422 We found significant linear correlation between each of the [HONO] techniques and
423 $[\text{HONO}]_{\text{ADS}}$ with a slope of ~ 1 . Note that the y-intercepts of Eq. (1)—(4) are much
424 smaller than the overall range of measured [HONO] (up to 121 ppbv). In addition, p-
425 values of the intercepts for all 4 fittings are much greater than 0.05, suggesting the
426 intercepts are not significantly different from zero. All data except one fall within 95%
427 confidence interval bounds of the overall fitting (Fig. 3). Therefore, we conclude that the
428 ADS method has high capture efficiency of HONO in the biomass combustion
429 environment, which assures the accuracy of the isotopic composition analysis and
430 applicability of this method for field-based biomass combustion research.

431

432 3.3 Isotopic composition of HONO and NO_x from burning different biomass

433

434 $\delta^{15}\text{N}$ of NO_x and HONO emitted from burning various biomass types in this study ranged
435 from $-4.3\text{‰} - +7.0\text{‰}$ and $-5.3 - +5.8\text{‰}$, respectively (Table 1). There is no direct
436 dependence of $\delta^{15}\text{N}$ on concentration of either HONO or NO_x (Figure S1). In Fig. 4, $\delta^{15}\text{N}$
437 values of NO_x and HONO are shown for each biomass type. Each value represents a
438 mean weighted by concentration (if multiple samples were collected for a biomass type)
439 with error bars representing propagation of replicate variation and method precision. For
440 biomass types burned in replicate (PIPO, PICO, PIEN, PSME), the $\delta^{15}\text{N}$ - NO_x and $\delta^{15}\text{N}$ -
441 HONO variation within a given biomass type is smaller than the full range across all fuel
442 types. Additionally, we note that the variations of $\delta^{15}\text{N}$ - NO_x and $\delta^{15}\text{N}$ -HONO for PIPO
443 and $\delta^{15}\text{N}$ -HONO for PIEN are larger than the method analytical precision of $\delta^{15}\text{N}$ - NO_x
444 (1.5‰) and $\delta^{15}\text{N}$ -HONO (0.5‰), respectively, which represents fire-by-fire variation
445 likely due to different combustion conditions and/or different fuel compositions. For
446 example, fuel moisture content derived from the original biomass weight and dry biomass
447 weight reveal that the PIPO burned in fire no.3 had more moisture content (48.1%) than
448 fire no.2 (32.1%), which could affect combustion temperature and thus product
449 formation. Fig. 4 also illustrates burning different biomass parts from specific vegetation
450 can result in fairly diverse $\delta^{15}\text{N}$ -HONO and $\delta^{15}\text{N}$ - NO_x , e.g. among PIPO mixture, canopy
451 and litter, as well as between PIEN mixture and duff.

452

453 Our $\delta^{15}\text{N}$ - NO_x range falls well within the range ($-7\text{‰} - +12\text{‰}$) found in the FLAME-4
454 experiment (Fibiger and Hastings, 2016). The FLAME-4 study investigated NO_x
455 emissions from burning a relatively large range of vegetation biomass from all over the
456 world, and found a linear relationship (Eq. (5)), indicating that 83% of the variation of



457 $\delta^{15}\text{N-NO}_x$ is explained by $\delta^{15}\text{N-biomass}$. The biomass types burned in this work focused
458 on vegetation in the western U.S., and differ greatly from that in FLAME-4, with
459 Ponderosa pine being the only common biomass between the two studies. Specifically,
460 the $\delta^{15}\text{N-biomass}$ range (-4.2‰ – +0.9‰) for this work is much narrower than that of the
461 FLAME-4 experiment (-8‰ – +8‰).

$$462 \delta^{15}\text{N-NO}_x = 0.41 \delta^{15}\text{N-biomass} + 1.0 \quad (r^2=0.83, p<0.001) \quad \text{Eq. (5)}$$

463
464
465 To compare with the relationship found in Fibiger and Hastings (2016), we mass
466 weighted the contributions from different components of the same biomass type. For the
467 same type of biomass, $\delta^{15}\text{N-biomass}$ varies amongst different parts of the vegetation with
468 differences as great as 4.1‰, 2.4‰, 4.6‰ and 2.6‰ for PIPO, PICO, PSME and PIEN,
469 respectively (Table S1). In the FIREX experiments, many of the burns were conducted
470 for mixtures of various vegetation parts. For instance, one PIPO fire contains canopy
471 (~30%), litter (~28%), and other parts (~42%) including duff and shrub, and the
472 compositions vary slightly amongst each burn. Therefore, the $\delta^{15}\text{N}$ of a particular
473 biomass mixture is mass weighted according to its composition contribution from each
474 part (Table S1). Similarly, the $\delta^{15}\text{N-NO}_x$ and $\delta^{15}\text{N-HONO}$ from fires of different biomass
475 parts are weighted by concentrations for each biomass type, i.e. PIPO (including mixture,
476 canopy and litter) and PIEN (including mixture and duff), to produce a signature
477 associated with combustion of that biomass type.

478
479 For purpose of comparison among different biomass types, we average $\delta^{15}\text{N-NO}_x$ ($\delta^{15}\text{N-}$
480 HONO) weighted by concentrations for each biomass type, i.e. PIPO (including mixture,
481 canopy and litter) and PIEN (including mixture and duff) (all data are listed in Table S3).
482 Linear regressions between $\delta^{15}\text{N-HONO}$ and $\delta^{15}\text{N-biomass}$, as well as that between $\delta^{15}\text{N-}$
483 NO_x and $\delta^{15}\text{N-biomass}$, show that both $\delta^{15}\text{N-HONO}$ and $\delta^{15}\text{N-NO}_x$ increase with $\delta^{15}\text{N-}$
484 biomass in general (Fig. S2). However, the linear regressions performed here are limited
485 by small datasets (4 data points each) and unsurprisingly yield insignificant linear
486 correlations for $\delta^{15}\text{N-HONO}$ (or $\delta^{15}\text{N-NO}_x$) versus $\delta^{15}\text{N-biomass}$ (p values are 0.1 and
487 0.5, respectively). Still, combining our results of $\delta^{15}\text{N-NO}_x$ versus $\delta^{15}\text{N-biomass}$ from
488 this work with those from the FLAME-4 study (Fibiger and Hastings, 2016) results in a
489 significant linear correlation (Eq. (6)) and is shown in Fig. 5. Despite differences in
490 burned biomass types between the two studies, our $\delta^{15}\text{N-NO}_x$ reasonably overlap with the
491 FLAME-4 results within our $\delta^{15}\text{N-biomass}$ range. The relationship between $\delta^{15}\text{N-NO}_x$
492 and $\delta^{15}\text{N-biomass}$ (Eq. (6)) for the combined data highly reproduces that obtained solely
493 from FLAME-4 study (Eq. (5)) and constrains the dependence of $\delta^{15}\text{N-NO}_x$ on $\delta^{15}\text{N-}$
494 biomass .

$$495 \delta^{15}\text{N-NO}_x = (0.42 \pm 0.17) \delta^{15}\text{N-biomass} + 1.3 \quad (r^2=0.71, p<0.001) \quad \text{Eq. (6)}$$

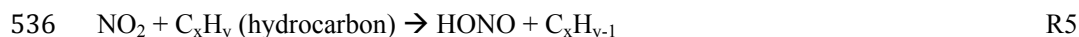
496
497
498 The mean values weighted by concentration plotted in Fig. 4 show ^{15}N of HONO is
499 consistently slightly more depleted than that of NO_x ($\delta^{15}\text{N-HONO} < \delta^{15}\text{N-NO}_x$) across all
500 the biomass types, except for PIPO-litter which results in an opposite relationship
501 between $\delta^{15}\text{N-HONO}$ and $\delta^{15}\text{N-NO}_x$. Furthermore, $\delta^{15}\text{N-HONO}$ is linearly correlated
502 with $\delta^{15}\text{N-NO}_x$ following a relationship of Eq. (7) within the $\delta^{15}\text{N-NO}_x$ and $\delta^{15}\text{N-HONO}$



503 range obtained in the current study (Fig. 6). This provides potential insights into HONO-
504 NO_x interactions and HONO formation pathways in fresh emissions from biomass
505 burning. Although a number of studies on wildfire biomass burning have suggested that
506 partitioning of N emissions between NO_x and NH₃ depends on combustion conditions
507 represented by MCE (Ferek et al., 1998; Goode et al., 1999; McMeeking et al., 2009;
508 Yokelson et al., 1996, 2008), HONO formation pathways remain unclear (Alvarado et al.,
509 2009, 2015; Nie et al., 2015).

$$510 \quad \delta^{15}\text{N-HONO} = 1.01 \delta^{15}\text{N-NO}_x - 1.52 \quad (R^2 = 0.89, p < 0.001) \quad \text{Eq. (7)}$$

511 Previous mechanistic studies on combustion of biomass/biofuel model compounds in a
512 well controlled closed system have investigated detailed nitrogen chemistry in the gas
513 phase, suggesting NO_x and HONO are formed from chain reactions involving oxidation
514 of precursors NH₃ and HCN, which are produced via devolatilization and pyrolysis of
515 amines and proteins in biomass/biofuel (Houshfar et al., 2012; Lucassen et al., 2011).
516 When the combustion conditions favor the oxidation of NH₃ and HCN, NO is first
517 formed and the chain reactions control the cycling of reactive nitrogen species (NO, NO₂
518 and HONO). Detailed and mechanistic nitrogen chemistry for the chemical relationship
519 between NO_x and HONO in the combustion environment have been discussed in earlier
520 works (Chai and Goldsmith, 2017; Shrestha et al., 2018; Skreiberg et al., 2004). In
521 addition, Houshfar et al. (2012) performed biomass combustion kinetic modeling with
522 reduced mechanism via sensitivity analysis. From these works, we extract major
523 pathways (R1-R11) that are likely responsible for fast gas-phase inter-conversion
524 between NO_x and HONO within the combustion system. They found whether HONO is
525 converted from NO or NO₂ in series during nitrogen transformation (referred to as
526 nitrogen flow) critically depends on temperature. Specifically, within 1 second of
527 residence time, at moderate temperatures (e.g. 700 °C), dominant nitrogen flow following
528 NO formation in biomass combustion is NO → NO₂ → HONO → NO, and major reactions
529 involving NO_x-HONO conversion are listed in R1-R6; at high temperatures (e.g. 850 °C
530 and above), the nitrogen flow cycle NO → HONO → NO₂ → NO becomes dominant, and
531 major reactions involving NO_x-HONO are R7-R11.





543 Although our studied fuels are more complicated in composition than a model system
544 involving no more than a few starting species, results from the above studies provide
545 fundamental underpinnings for biomass combustion. Also note that heterogeneous
546 chemistry after these species were emitted was not considered here as the residence time
547 of the fresh plume in our study was ~5 seconds, which is of the same magnitude as that
548 predicted in the nitrogen flow analysis (Houshfar et al., 2012). Kinetic isotope effects
549 (KIE) of these reactions have not been characterized; so only a semi-quantitative
550 prediction is presented here. At low temperatures, R1-R5 are all H-abstraction reactions
551 involving loose transition states that have significant activation energy; a primary KIE is
552 expected for such conditions and leads to ^{15}N depletion in the product (HONO) (Chai et
553 al., 2014; Matsson and Westaway, 1999, and references therein). Additionally, R6 is a
554 unimolecular dissociation reaction with no reaction barrier, and hence R6 could be
555 expected to have a small kinetic isotope effect enriching ^{15}N in HONO, somewhat
556 offsetting the depletion that arose from R1-R5. Consequently, the overall isotope effect of
557 R1-R6 would lead to $\delta^{15}\text{N-HONO} < \delta^{15}\text{N-NO}_x$ by a small difference, consistent with our
558 results (Fig. 4). On the other hand, the KIE for the reactions R7-R11 at higher
559 temperatures ($> 850\text{ }^\circ\text{C}$) is expected to enrich ^{15}N in HONO relative to NO_x (Chai and
560 Dibble, 2014), leading to an opposite isotope effect to that predicted at lower
561 temperatures.

562 Temperatures of the biomass combustion process span a large range involving different
563 processes including preheating, drying, distillation, pyrolysis, gasification (aka “glowing
564 combustion”) and oxidation in turbulent diffusion flames at a range of temperatures
565 associated with changing flame dynamics (Yokelson et al., 1996). Despite this
566 complexity, our measured slight ^{15}N enrichment in NO_x compared to HONO (Table 1,
567 Fig. 4) suggests that the reactions R1-R6 play a more important role than R7-R11 in
568 HONO formation during the FIREX Fire Lab experiments.

569

570 **3.4 Isotopic composition of nitrates collected on particle filters**

571 All Nylasorb filter extract solutions showed no detectable NO_3^- and NO_2^- concentrations,
572 indicating no significant amount of HNO_3 was collected on these filters, which is
573 consistent with the very low concentrations measured by MC/IC (note that low
574 concentration and limited sample volume also preclude further isotopic analysis of HNO_3
575 collected by MC/IC). By contrast, we found 5 out of 20 particulate filter extract solutions
576 had detectable NO_3^- concentration that were sufficient (10 nmol N) for isotopic
577 composition analysis (Table 1). $\delta^{15}\text{N}$ and $\delta^{18}\text{O}$ reported here are considered to represent
578 $\text{NO}_3^-(\text{p})$. $\delta^{15}\text{N-NO}_3^-(\text{p})$ of the five samples (burns) range from -10.6 to -7.4 ‰, all of
579 which are more ^{15}N depleted than that of HONO and NO_x . In addition, the smaller range of
580 of $\delta^{15}\text{N-NO}_3^-$ than that of $\delta^{15}\text{N-HONO}$ and $\delta^{15}\text{N-NO}_x$ rules out possible transformation of



581 NO_x and HONO to nitrate on the filters, which could distort the isotopic composition of
582 NO_x and HONO.

583

584 In the FLAME-4 experiments (Fibiger and Hastings, 2016), only one particulate filter had
585 captured NO₃⁻(p) above the concentration detection limit, whereas HNO₃ collected on
586 Nylasorb filters from 7 experiments were above the concentration detection limit and
587 therefore only δ¹⁵N-HNO₃ (-0.3 – 11.2‰) were reported. The contrast with our filter
588 results are likely attributed to different formation mechanisms under different conditions,
589 in addition to variation of fuel types. Of the 7 detectable HNO₃ collections from FLAME-
590 4, 5 represented room burns for which samples were collected from smoke aged for 1-2
591 hours in the lab, and the sampled HNO₃ was likely a secondary product. By contrast all
592 our observed NO₃⁻(p) were in fresh emissions and may have been derived from plant
593 nitrate (Cárdenas-Navarro et al., 1999) and/or combustion reactions. There have been no
594 other studies on δ¹⁵N of NO₃⁻(p) and HNO₃ directly emitted from fresh plumes to the best
595 of our knowledge, so more investigation using both laboratory work (isotope effect) and
596 kinetic modeling will be needed in order to understand formation mechanisms of HNO₃
597 and NO₃⁻(p) in the biomass combustion process and their respective isotope effects.

598

599 In addition to δ¹⁵N, we report δ¹⁸O of HONO and NO₃⁻(p) directly emitted from biomass
600 burning plumes with ranges of 5.2‰ – 15.2‰ and 11.5‰ – 14.8‰, respectively. These
601 are the first observations reported for δ¹⁸O of reactive nitrogen species directly emitted
602 from biomass burning and low values are expected for the δ¹⁸O, which, in this case, is
603 mainly extracted from that of molecular oxygen (δ¹⁸O = ~23.5‰) (Kroopnick and Craig,
604 1972), biomass/cellulose (δ¹⁸O = 15‰–35‰), and/or biomass contained water (δ¹⁸O = ~
605 0‰– 16‰) (Keel et al., 2016). In field studies where photochemistry and O₃ are
606 inevitably involved in the reactive nitrogen cycle in various stages of aged plumes, we
607 expect to see much more elevated δ¹⁸O values of HONO and NO₃⁻(p) due to the
608 extremely high value of δ¹⁸O-O₃ (~110‰) (Vicars and Savarino, 2014). Therefore, the
609 δ¹⁸O found in the lab is helpful in understanding conditions where photochemistry would
610 not apply (e.g. nighttime fresh smoke) and should be distinguishable from the expected
611 higher δ¹⁸O that would be found in aged smoke and/or daytime fresh smoke.

612

613 4 Conclusions

614

615 In this study we applied new methods for characterizing the isotopic composition of
616 reactive nitrogen species including NO_x (δ¹⁵N), HONO (δ¹⁵N and δ¹⁸O), and NO₃⁻(p)
617 (δ¹⁵N and δ¹⁸O) emitted directly from biomass burning. We measured fresh (stack)
618 emissions from 20 laboratory fires of different fuels during the 2016 FIREX Fire Lab
619 experiments. NO_x, HONO and HNO₃ emitted in fresh smoke reached their peak in most
620 of our fires within five minutes of ignition of biomass (i.e. when flaming combustion
621 peaked). The HONO mixing ratio was typically ~2 orders of magnitude larger than
622 HNO₃, and HONO/NO_x ratio ranged from 0.13 to 0.53.

623

624 Our HONO collection method (ADS) for isotopic analysis was applied to biomass
625 burning (BB) for the first time. The good agreement for concentration comparison
626 between our method and 4 high time-resolution HONO concentration methods suggests



627 high collection efficiency of HONO from BB emissions, which ensures accurate isotopic
628 compositional analysis. Comparison with concurrent observations and a previous study
629 show that the combination of our HONO and NO_x collection methods are compatible,
630 allowing for simultaneous determination of the isotopic composition of both HONO and
631 NO_x. This provides important potential for investigating the photochemical and non-
632 photochemical relationships between HONO and NO_x in a variety of environments, and
633 especially in BB plumes.

634
635 $\delta^{15}\text{N-NO}_x$ emitted from burning various Western U.S. biomass types in this study ranged
636 from -4.3 ‰ to +7.0 ‰, falling well within the range found by (Fibiger and Hastings,
637 2016), although the vegetation types were much broader in the earlier study. We report
638 the first $\delta^{15}\text{N-HONO}$ emitted directly from burning, ranging from -5.3 to +5.8‰. $\delta^{15}\text{N-}$
639 NO_x and $\delta^{15}\text{N-HONO}$ range derived from BB can be further compared with that from
640 other sources using the same methods presented here, and provide insights into source
641 signatures for both NO_x and HONO. This study also showed the important capability of
642 determining $\delta^{18}\text{O-HONO}$ and $\delta^{18}\text{O-NO}_3^-(\text{p})$ from BB plumes, and we expect $\delta^{18}\text{O}$ of both
643 HONO and NO₃⁻(p) produced under photochemical conditions will be much higher than
644 the lab results due to the important role of O₃ in reactive nitrogen oxidation.

645
646 Interestingly, the linear correlation between $\delta^{15}\text{N-HONO}$ and $\delta^{15}\text{N-NO}_x$ for the biomass
647 we studied suggests systematic co-produced NO_x and HONO occurs in the combustion
648 and both of them are released as primary pollutants in fresh smoke. The relationship
649 between $\delta^{15}\text{N-HONO}$ and $\delta^{15}\text{N-NO}_x$ likely reflects the gas phase biomass combustion
650 process for flow of reactive nitrogen species at moderate combustion temperatures (< 800
651 °C). This correlation is potentially useful to distinguish HONO sources and formation
652 pathways in the environment. Determining these relationships in real wildfire smoke will
653 be essential for better constraint on NO_x and HONO budgets, and eventually may
654 improve ozone and secondary aerosol predictions for regional air quality.



Data availability. The data from the laboratory tests are available on request from the corresponding authors. Data from the 2016 Missoula Fire lab are available here: <https://esrl.noaa.gov/csd/groups/csd7/measurements/2016firex/FireLab/DataDownload/>

Supplement.

Author contribution. JC, MH and JD designed this work. JC and DJM conducted the sample collections at the Fire Lab, with additional support from MH, JD and ES. JC carried out the isotopic composition measurements; DJM supported the isotopic research and interpretation. ES helped analyze the MC/IC data. VS and RY provided the OP-FTIR data. KJZ and SSB provided the ACES data. ARK and CW provided the PTR-ToF data. JC wrote the manuscript, and all authors provided edits and feedback.

Competing interests. The authors declare that they have no conflicts of interest.

Acknowledgement. This work was supported by funding from the National Oceanic and Atmospheric Administration (AC4 Award NA16OAR4310098 to MH) and the National Science Foundation (AGS-1351932 to MH). The FIREX Fire Lab study was supported in part by the NOAA Climate Office's Atmospheric Chemistry, Carbon Cycle, and Climate program. We are grateful for Ruby Ho for laboratory support and Marshall Otter for the biomass $\delta^{15}\text{N}$ analysis. We also thank James Roberts and Matthew Coggon for helpful discussions.

References

- Akagi, S. K., Craven, J. S., Taylor, J. W., McMeeking, G. R., Yokelson, R. J., Burling, I. R., Urbanski, S. P., Wold, C. E., Seinfeld, J. H., Coe, H., Alvarado, M. J. and Weise, D. R.: Evolution of trace gases and particles emitted by a chaparral fire in California, *Atmos Chem Phys*, 12(3), 1397–1421, doi:10.5194/acp-12-1397-2012, 2012.
- Akagi, S. K., Yokelson, R. J., Burling, I. R., Meinardi, S., Simpson, I., Blake, D. R., McMeeking, G. R., Sullivan, A., Lee, T., Kreidenweis, S., Urbanski, S., Reardon, J., Griffith, D. W. T., Johnson, T. J. and Weise, D. R.: Measurements of reactive trace gases and variable O₃ formation rates in some South Carolina biomass burning plumes, *Atmos Chem Phys*, 13(3), 1141–1165, doi:10.5194/acp-13-1141-2013, 2013.
- Alvarado, M. J. and Prinn, R. G.: Formation of ozone and growth of aerosols in young smoke plumes from biomass burning: 1. Lagrangian parcel studies, *J. Geophys. Res. Atmospheres*, 114(D9), doi:10.1029/2008JD011144, 2009.



Alvarado, M. J., Wang, C. and Prinn, R. G.: Formation of ozone and growth of aerosols in young smoke plumes from biomass burning: 2. Three-dimensional Eulerian studies, *J. Geophys. Res. Atmospheres*, 114(D9), doi:10.1029/2008JD011186, 2009.

Alvarado, M. J., Lonsdale, C. R., Yokelson, R. J., Akagi, S. K., Coe, H., Craven, J. S., Fischer, E. V., McMeeking, G. R., Seinfeld, J. H., Soni, T., Taylor, J. W., Weise, D. R. and Wold, C. E.: Investigating the links between ozone and organic aerosol chemistry in a biomass burning plume from a prescribed fire in California chaparral, *Atmos Chem Phys*, 15(12), 6667–6688, doi:10.5194/acp-15-6667-2015, 2015.

Böhlke, J. K., Mroczkowski, S. J. and Coplen, T. B.: Oxygen isotopes in nitrate: new reference materials for 18O:17O:16O measurements and observations on nitrate-water equilibration, *Rapid Commun. Mass Spectrom.*, 17(16), 1835–1846, doi:10.1002/rcm.1123, 2003.

Burling, I. R., Yokelson, R. J., Griffith, D. W. T., Johnson, T. J., Veres, P., Roberts, J. M., Warneke, C., Urbanski, S. P., Reardon, J., Weise, D. R., Hao, W. M. and de Gouw, J.: Laboratory measurements of trace gas emissions from biomass burning of fuel types from the southeastern and southwestern United States, *Atmos Chem Phys*, 10(22), 11115–11130, doi:10.5194/acp-10-11115-2010, 2010.

Burling, I. R., Yokelson, R. J., Akagi, S. K., Urbanski, S. P., Wold, C. E., Griffith, D. W. T., Johnson, T. J., Reardon, J. and Weise, D. R.: Airborne and ground-based measurements of the trace gases and particles emitted by prescribed fires in the United States, *Atmos Chem Phys*, 11(23), 12197–12216, doi:10.5194/acp-11-12197-2011, 2011.

Cárdenas-Navarro, R., Adamowicz, S. and Robin, P.: Nitrate accumulation in plants: a role for water, *J. Exp. Bot.*, 50(334), 613–624, doi:10.1093/jxb/50.334.613, 1999.

Casciotti, K. L., Sigman, D. M., Hastings, M. G., Böhlke, J. K. and Hilkert, A.: Measurement of the Oxygen Isotopic Composition of Nitrate in Seawater and Freshwater Using the Denitrifier Method, *Anal. Chem.*, 74(19), 4905–4912, doi:10.1021/ac020113w, 2002.

Chai, J. and Dibble, T. S.: Pressure Dependence and Kinetic Isotope Effects in the Absolute Rate Constant for Methoxy Radical Reacting with NO₂, *Int. J. Chem. Kinet.*, 46(9), 501–511, doi:10.1002/kin.20865, 2014.

Chai, J. and Goldsmith, C. F.: Rate coefficients for fuel + NO₂: Predictive kinetics for HONO and HNO₂ formation, *Proc. Combust. Inst.*, 36(1), 617–626, doi:10.1016/j.proci.2016.06.133, 2017.

Chai, J. and Hastings, M.: Collection Method for Isotopic Analysis of Gaseous Nitrous Acid, *Anal. Chem.*, 90(1), 830–838, doi:10.1021/acs.analchem.7b03561, 2018.



- Chai, J., Hu, H., Dibble, T. S., Tyndall, G. S. and Orlando, J. J.: Rate Constants and Kinetic Isotope Effects for Methoxy Radical Reacting with NO₂ and O₂, *J. Phys. Chem. A*, 118(20), 3552–3563 [online] Available from: <http://pubs.acs.org/doi/abs/10.1021/jp501205d> (Accessed 24 June 2015), 2014.
- Christian, T. J., Kleiss, B., Yokelson, R. J., Holzinger, R., Crutzen, P. J., Hao, W. M., Shirai, T. and Blake, D. R.: Comprehensive laboratory measurements of biomass-burning emissions: 2. First intercomparison of open-path FTIR, PTR-MS, and GC-MS/FID/ECD, *J. Geophys. Res. Atmospheres*, 109(D2), doi:10.1029/2003JD003874, 2004.
- Cook, P. A., Savage, N. H., Turquety, S., Carver, G. D., O'Connor, F. M., Heckel, A., Stewart, D., Whalley, L. K., Parker, A. E., Schlager, H., Singh, H. B., Avery, M. A., Sachse, G. W., Brune, W., Richter, A., Burrows, J. P., Purvis, R., Lewis, A. C., Reeves, C. E., Monks, P. S., Levine, J. G. and Pyle, J. A.: Forest fire plumes over the North Atlantic: p-TOMCAT model simulations with aircraft and satellite measurements from the ITOP/ICARTT campaign, *J. Geophys. Res. Atmospheres*, 112, D10S43, doi:10.1029/2006JD007563, 2007.
- Crutzen, P. J. and Andreae, M. O.: Biomass burning in the tropics: impact on atmospheric chemistry and biogeochemical cycles, *Science*, 250(4988), 1669–1678, doi:10.1126/science.250.4988.1669, 1990.
- Dibb, J. E., Arsenault, M., Peterson, M. C. and Honrath, R. E.: Fast nitrogen oxide photochemistry in Summit, Greenland snow, *Atmos. Environ.*, 36(15–16), 2501–2511, doi:10.1016/S1352-2310(02)00130-9, 2002.
- Ferek, R., Reid, J., Hobbs, P., Blake, D. and Liousse, C.: Emission factors of hydrocarbons, halocarbons, trace gases and particles from biomass burning in Brazil, *J. Geophys. Res.-ATMOSPHERES*, 103, 32107–32118, doi:10.1029/98JD00692, 1998.
- Fibiger, D. L. and Hastings, M. G.: First Measurements of the Nitrogen Isotopic Composition of NO_x from Biomass Burning, *Environ. Sci. Technol.*, 50(21), 11569–11574, doi:10.1021/acs.est.6b03510, 2016.
- Fibiger, D. L., Hastings, M. G., Lew, A. F. and Peltier, R. E.: Collection of NO and NO₂ for Isotopic Analysis of NO_x Emissions, *Anal. Chem.*, 86(24), 12115–12121, doi:10.1021/ac502968e, 2014.
- FIREX: FIREX 2016 Fire Lab Data Archive, [online] Available from: <https://esrl.noaa.gov/csd/groups/csd7/measurements/2016firex/FireLab/DataDownload/index.php?page=/csd/groups/csd7/measurements/2016firex/FireLab/DataDownload/> (Accessed 25 March 2019), 2016.
- Goode, J. G., Yokelson, R. J., Susott, R. A. and Ward, D. E.: Trace gas emissions from laboratory biomass fires measured by open-path Fourier transform infrared



spectroscopy: Fires in grass and surface fuels, *J. Geophys. Res.*, 104, 21, doi:10.1029/1999JD900360, 1999.

Hastings, M. G., Casciotti, K. L. and Elliott, E. M.: Stable Isotopes as Tracers of Anthropogenic Nitrogen Sources, Deposition, and Impacts, *Elements*, 9(5), 339–344, doi:10.2113/gselements.9.5.339, 2013.

Houshfar, E., Skreiberg, Ø., Glarborg, P. and Løvås, T.: Reduced chemical kinetic mechanisms for NO_x emission prediction in biomass combustion, *Int. J. Chem. Kinet.*, 4(44), 219–231, doi:10.1002/kin.20716, 2012.

Jaeglé, L., Steinberger, L., Martin, R. V. and Chance, K.: Global partitioning of NO_x sources using satellite observations: relative roles of fossil fuel combustion, biomass burning and soil emissions, *Faraday Discuss.*, 130, 407–423; discussion 491–517, 519–524, 2005.

Jaffe, D. and Briggs, N.: Ozone production from wildfires: A critical review, *Atmos. Environ.*, 51, 1–10, doi:10.1016/j.atmosenv.2011.11.063, 2012.

Keel, S. G., Joos, F., Spahni, R., Saurer, M., Weigt, R. B. and Klesse, S.: Simulating oxygen isotope ratios in tree ring cellulose using a dynamic global vegetation model, *Biogeosciences*, 13(13), 3869–3886, doi:https://doi.org/10.5194/bg-13-3869-2016, 2016.

Keene, W. C., Lobert, J. M., Crutzen, P. J., Maben, J. R., Scharffe, D. H., Landmann, T., Hély, C. and Brain, C.: Emissions of major gaseous and particulate species during experimental burns of southern African biomass, *J. Geophys. Res. Atmospheres*, 111(D4), doi:10.1029/2005JD006319, 2006.

Koss, A. R., Sekimoto, K., Gilman, J. B., Selimovic, V., Coggon, M. M., Zarzana, K. J., Yuan, B., Lerner, B. M., Brown, S. S., Jimenez, J. L., Krechmer, J., Roberts, J. M., Warneke, C., Yokelson, R. J. and Gouw, J. de: Non-methane organic gas emissions from biomass burning: identification, quantification, and emission factors from PTR-ToF during the FIREX 2016 laboratory experiment, *Atmospheric Chem. Phys.*, 18(5), 3299–3319, doi:https://doi.org/10.5194/acp-18-3299-2018, 2018.

Kraus, S.: DOASIS: a framework design for DOAS., 2006.

Kroopnick, P. and Craig, H.: Atmospheric oxygen: isotopic composition and solubility fractionation, *Science*, 175(4017), 54–55, doi:10.1126/science.175.4017.54, 1972.

Lapina, K., Honrath R. E., Owen R. C., Val Martín M., Hyer E. J. and Fialho P.: Late summer changes in burning conditions in the boreal regions and their implications for NO_x and CO emissions from boreal fires, *J. Geophys. Res. Atmospheres*, 113(D11), doi:10.1029/2007JD009421, 2008.



Liu, X., Zhang, Y., Huey, L. G., Yokelson, R. J., Wang, Y., Jimenez, J. L., Campuzano-Jost, P., Beyersdorf, A. J., Blake, D. R., Choi, Y., Clair, J. M. S., Crouse, J. D., Day, D. A., Diskin, G. S., Fried, A., Hall, S. R., Hanisco, T. F., King, L. E., Meinardi, S., Mikoviny, T., Palm, B. B., Peischl, J., Perring, A. E., Pollack, I. B., Ryerson, T. B., Sachse, G., Schwarz, J. P., Simpson, I. J., Tanner, D. J., Thornhill, K. L., Ullmann, K., Weber, R. J., Wennberg, P. O., Wisthaler, A., Wolfe, G. M. and Ziemba, L. D.: Agricultural fires in the southeastern U.S. during SEAC4RS: Emissions of trace gases and particles and evolution of ozone, reactive nitrogen, and organic aerosol, *J. Geophys. Res. Atmospheres*, 121(12), 7383–7414, doi:10.1002/2016JD025040, 2016.

Lucassen, A., Labbe, N., Westmoreland, P. R. and Kohse-Höinghaus, K.: Combustion chemistry and fuel-nitrogen conversion in a laminar premixed flame of morpholine as a model biofuel, *Combust. Flame*, 158(9), 1647–1666, doi:10.1016/j.combustflame.2011.02.010, 2011.

Matsson, O. and Westaway, K. C.: Secondary Deuterium Kinetic Isotope Effects and Transition State Structure, in *Advances in Physical Organic Chemistry*, vol. 31, edited by D. Bethell, pp. 143–248, Academic Press., 1999.

McMeeking, G. R., Kreidenweis, S. M., Baker, S., Carrico, C. M., Chow, J. C., Collett, J. L., Hao, W. M., Holden, A. S., Kirchstetter, T. W., Malm, W. C., Moosmüller, H., Sullivan, A. P. and Wold, C. E.: Emissions of trace gases and aerosols during the open combustion of biomass in the laboratory, *J. Geophys. Res. Atmospheres*, 114(D19), D19210, doi:10.1029/2009JD011836, 2009.

Miller, D. J., Wojtal, P. K., Clark, S. C. and Hastings, M. G.: Vehicle NO_x emission plume isotopic signatures: Spatial variability across the eastern United States, *J. Geophys. Res. Atmospheres*, 122(8), 4698–4717, doi:10.1002/2016JD025877, 2017.

Miller, D. J., Chai, J., Guo, F., Dell, C. J., Karsten, H. and Hastings, M. G.: Isotopic Composition of In Situ Soil NO_x Emissions in Manure-Fertilized Cropland, *Geophys. Res. Lett.*, 45(21), 12,058–12,066, doi:10.1029/2018GL079619, 2018.

Min, K.-E., Washenfelder, R. A., Dubé, W. P., Langford, A. O., Edwards, P. M., Zarzana, K. J., Stutz, J., Lu, K., Rohrer, F., Zhang, Y. and Brown, S. S.: A broadband cavity enhanced absorption spectrometer for aircraft measurements of glyoxal, methylglyoxal, nitrous acid, nitrogen dioxide, and water vapor, *Atmospheric Meas. Tech.*, 9(2), 423–440, doi:https://doi.org/10.5194/amt-9-423-2016, 2016.

Neuman, J. A., Trainer, M., Brown, S. S., Min, K.-E., Nowak, J. B., Parrish, D. D., Peischl, J., Pollack, I. B., Roberts, J. M., Ryerson, T. B. and Veres, P. R.: HONO emission and production determined from airborne measurements over the Southeast U.S., *J. Geophys. Res. Atmospheres*, 121(15), 9237–9250, doi:10.1002/2016JD025197, 2016.

Nie, W., Ding, A. J., Xie, Y. N., Xu, Z., Mao, H., Kerminen, V.-M., Zheng, L. F., Qi, X. M., Huang, X., Yang, X.-Q., Sun, J. N., Herrmann, E., Petäjä, T., Kulmala, M. and Fu, C. B.:



- Influence of biomass burning plumes on HONO chemistry in eastern China, *Atmos Chem Phys*, 15(3), 1147–1159, doi:10.5194/acp-15-1147-2015, 2015.
- Perrino, C., De Santis, F. and Febo, A.: Criteria for the choice of a denuder sampling technique devoted to the measurement of atmospheric nitrous and nitric acids, *Atmospheric Environ. Part Gen. Top.*, 24(3), 617–626, doi:10.1016/0960-1686(90)90017-H, 1990.
- Pinto, J. P., Dibb, J., Lee, B. H., Rappenglück, B., Wood, E. C., Levy, M., Zhang, R.-Y., Lefer, B., Ren, X.-R., Stutz, J., Tsai, C., Ackermann, L., Golovko, J., Herndon, S. C., Oakes, M., Meng, Q.-Y., Munger, J. W., Zahniser, M. and Zheng, J.: Intercomparison of field measurements of nitrous acid (HONO) during the SHARP campaign, *J. Geophys. Res. Atmospheres*, 119(9), 5583–5601, doi:10.1002/2013JD020287, 2014.
- Reed, C., Evans, M. J., Carlo, P. D., Lee, J. D. and Carpenter, L. J.: Interferences in photolytic NO₂ measurements: explanation for an apparent missing oxidant?, *Atmospheric Chem. Phys.*, 16(7), 4707–4724, doi:https://doi.org/10.5194/acp-16-4707-2016, 2016.
- Reinhardt, E. D., Keane, R. E. and Brown, J. K.: First Order Fire Effects Model: FOFEM 4.0, user's guide, Gen Tech Rep INT-GTR-344 Ogden UT US Dep. Agric. For. Serv. Intermt. Res. Stn. 65 P, 344, doi:10.2737/INT-GTR-344, 1997.
- Roberts, J. M., Veres, P., Warneke, C., Neuman, J. A., Washenfelder, R. A., Brown, S. S., Baasandorj, M., Burkholder, J. B., Burling, I. R., Johnson, T. J., Yokelson, R. J. and de Gouw, J.: Measurement of HONO, HNCO, and other inorganic acids by negative-ion proton-transfer chemical-ionization mass spectrometry (NI-PT-CIMS): application to biomass burning emissions, *Atmos Meas Tech*, 3(4), 981–990, doi:10.5194/amt-3-981-2010, 2010.
- Scheuer, E., Talbot, R. W., Dibb, J. E., Seid, G. K., DeBell, L. and Lefer, B.: Seasonal distributions of fine aerosol sulfate in the North American Arctic basin during TOPSE, *J. Geophys. Res. Atmospheres*, 108(D4), doi:10.1029/2001JD001364, 2003.
- Selimovic, V., Yokelson, R. J., Warneke, C., Roberts, J. M., de Gouw, J., Reardon, J. and Griffith, D. W. T.: Aerosol optical properties and trace gas emissions by PAX and OP-FTIR for laboratory-simulated western US wildfires during FIREX, *Atmos Chem Phys*, 18(4), 2929–2948, doi:10.5194/acp-18-2929-2018, 2018.
- Shrestha, K. P., Seidel, L., Zeuch, T. and Mauss, F.: Detailed Kinetic Mechanism for the Oxidation of Ammonia Including the Formation and Reduction of Nitrogen Oxides, *Energy Fuels*, doi:10.1021/acs.energyfuels.8b01056, 2018.
- Sigman, D. M., Casciotti, K. L., Andreani, M., Barford, C., Galanter, M. and Böhlke, J. K.: A Bacterial Method for the Nitrogen Isotopic Analysis of Nitrate in Seawater and Freshwater, *Anal. Chem.*, 73(17), 4145–4153, doi:10.1021/ac010088e, 2001.



Skreiberg, Ø., Kilpinen, P. and Glarborg, P.: Ammonia chemistry below 1400 K under fuel-rich conditions in a flow reactor, *Combust. Flame*, 136(4), 501–518, doi:10.1016/j.combustflame.2003.12.008, 2004.

Stockwell, C. E., Yokelson, R. J., Kreidenweis, S. M., Robinson, A. L., DeMott, P. J., Sullivan, R. C., Reardon, J., Ryan, K. C., Griffith, D. W. T. and Stevens, L.: Trace gas emissions from combustion of peat, crop residue, domestic biofuels, grasses, and other fuels: configuration and Fourier transform infrared (FTIR) component of the fourth Fire Lab at Missoula Experiment (FLAME-4), *Atmos Chem Phys*, 14(18), 9727–9754, doi:10.5194/acp-14-9727-2014, 2014.

Stutz, J., Oh, H.-J., Whitlow, S. I., Anderson, C., Dibb, J. E., Flynn, J. H., Rappenglück, B. and Lefer, B.: Simultaneous DOAS and mist-chamber IC measurements of HONO in Houston, TX, *Atmos. Environ.*, 44(33), 4090–4098, doi:10.1016/j.atmosenv.2009.02.003, 2010.

Tkacik, D. S., Robinson, E. S., Ahern, A., Saleh, R., Stockwell, C., Veres, P., Simpson, I. J., Meinardi, S., Blake, D. R., Yokelson, R. J., Presto, A. A., Sullivan, R. C., Donahue, N. M. and Robinson, A. L.: A dual-chamber method for quantifying the effects of atmospheric perturbations on secondary organic aerosol formation from biomass burning emissions, *J. Geophys. Res. Atmospheres*, 122(11), 6043–6058, doi:10.1002/2016JD025784, 2017.

Travis, K. R., Jacob, D. J., Fisher, J. A., Kim, P. S., Marais, E. A., Zhu, L., Yu, K., Miller, C. C., Yantosca, R. M., Sulprizio, M. P., Thompson, A. M., Wennberg, P. O., Crounse, J. D., St. Clair, J. M., Cohen, R. C., Laughner, J. L., Dibb, J. E., Hall, S. R., Ullmann, K., Wolfe, G. M., Pollack, I. B., Peischl, J., Neuman, J. A. and Zhou, X.: Why do models overestimate surface ozone in the Southeast United States?, *Atmos Chem Phys*, 16(21), 13561–13577, doi:10.5194/acp-16-13561-2016, 2016.

Trentmann, J., Yokelson, R. J., Hobbs, P. V., Winterrath, T., Christian, T. J., Andreae, M. O. and Mason, S. A.: An analysis of the chemical processes in the smoke plume from a savanna fire, *J. Geophys. Res. Atmospheres*, 110(D12), doi:10.1029/2004JD005628, 2005.

Val Martín, M., Honrath, R. E., Owen, R. C., Pfister, G., Fialho, P. and Barata, F.: Significant enhancements of nitrogen oxides, black carbon, and ozone in the North Atlantic lower free troposphere resulting from North American boreal wildfires, *J. Geophys. Res. Atmospheres*, 111(D23), doi:10.1029/2006JD007530, 2006.

Veres, P., Roberts, J. M., Burling, I. R., Warneke, C., Gouw, J. de and Yokelson, R. J.: Measurements of gas-phase inorganic and organic acids from biomass fires by negative-ion proton-transfer chemical-ionization mass spectrometry, *J. Geophys. Res. Atmospheres*, 115(D23), doi:10.1029/2010JD014033, 2010.

Vicars, W. C. and Savarino, J.: Quantitative constraints on the 17O-excess ($\Delta 17\text{O}$) signature of surface ozone: Ambient measurements from 50°N to 50°S using the



nitrite-coated filter technique, *Geochim. Cosmochim. Acta*, 135(Supplement C), 270–287, doi:10.1016/j.gca.2014.03.023, 2014.

Wojtal, P. K., Miller, D. J., O’Conner, M., Clark, S. C. and Hastings, M. G.: Automated, High-resolution Mobile Collection System for the Nitrogen Isotopic Analysis of NO_x, *J. Vis. Exp. JoVE*, (118), doi:10.3791/54962, 2016.

Ye, C., Zhou, X., Pu, D., Stutz, J., Festa, J., Spolaor, M., Tsai, C., Cantrell, C., Mauldin, R. L., Campos, T., Weinheimer, A., Hornbrook, R. S., Apel, E. C., Guenther, A., Kaser, L., Yuan, B., Karl, T., Haggerty, J., Hall, S., Ullmann, K., Smith, J. N., Ortega, J. and Knote, C.: Rapid cycling of reactive nitrogen in the marine boundary layer, *Nature*, 532(7600), 489–491, doi:10.1038/nature17195, 2016.

Yokelson, R., W. T. Griffith, D. and Ward, D.: Open-path Fourier transform infrared studies of large-scale laboratory biomass fires, *J. Geophys. Res.*, 101, 21067, doi:10.1029/96JD01800, 1996.

Yokelson, R. J., Karl, T., Artaxo, P., Blake, D. R., Christian, T. J., Griffith, D. W. T., Guenther, A. and Hao, W. M.: The Tropical Forest and Fire Emissions Experiment: overview and airborne fire emission factor measurements, *Atmos Chem Phys*, 7(19), 5175–5196, doi:10.5194/acp-7-5175-2007, 2007.

Yokelson, R. J., Christian, T. J., Karl, T. G. and Guenther, A.: The tropical forest and fire emissions experiment: laboratory fire measurements and synthesis of campaign data, *Atmos Chem Phys*, 8(13), 3509–3527, doi:10.5194/acp-8-3509-2008, 2008.

Yokelson, R. J., Crounse, J. D., DeCarlo, P. F., Karl, T., Urbanski, S., Atlas, E., Campos, T., Shinozuka, Y., Kapustin, V., Clarke, A. D., Weinheimer, A., Knapp, D. J., Montzka, D. D., Holloway, J., Weibring, P., Flocke, F., Zheng, W., Toohey, D., Wennberg, P. O., Wiedinmyer, C., Mauldin, L., Fried, A., Richter, D., Walega, J., Jimenez, J. L., Adachi, K., Buseck, P. R., Hall, S. R. and Shetter, R.: Emissions from biomass burning in the Yucatan, *Atmos Chem Phys*, 9(15), 5785–5812, doi:10.5194/acp-9-5785-2009, 2009.

Yuan, B., Koss, A., Warneke, C., Gilman, J. B., Lerner, B. M., Stark, H. and Gouw, J. A. de: A high-resolution time-of-flight chemical ionization mass spectrometer utilizing hydronium ions (H₃O⁺ ToF-CIMS) for measurements of volatile organic compounds in the atmosphere, *Atmospheric Meas. Tech.*, 9(6), 2735–2752, doi:<https://doi.org/10.5194/amt-9-2735-2016>, 2016.

Zarzana, K. J., Selimovic, V., Koss, A. R., Sekimoto, K., Coggon, M. M., Yuan, B., Dubé, W. P., Yokelson, R. J., Warneke, C., Gouw, J. A. de, Roberts, J. M. and Brown, S. S.: Primary emissions of glyoxal and methylglyoxal from laboratory measurements of open biomass burning, *Atmospheric Chem. Phys.*, 18(20), 15451–15470, doi:<https://doi.org/10.5194/acp-18-15451-2018>, 2018.



Zhou, S., Young, C. J., VandenBoer, T. C., Kowal, S. F. and Kahan, T. F.: Time-Resolved Measurements of Nitric Oxide, Nitrogen Dioxide, and Nitrous Acid in an Occupied New York Home, *Environ. Sci. Technol.*, 52(15), 8355–8364, doi:10.1021/acs.est.8b01792, 2018.



Table 1. Concentration (mean, derived from solution concentration and flow rate) and N isotopic composition for various biomass burning experiments, unit for all δ denotations is ‰. MCE values are extracted from NOAA FIREX fire archive. Note: fire no. 1, 7 and 13 were missing due to technical issues; NO_x results are only shown when blank/sample ratio is <70%. Biomass acronyms are defined in Sect. 2.1; in addition, d—duff, c—canopy, l—litter.

Biomass	Fire no.	HONO (ppbv)	$\delta^{15}\text{N}$ -HONO	$\delta^{18}\text{O}$ -HONO	NO _x (ppbv)	$\delta^{15}\text{N}$ -NO _x	$\delta^{15}\text{N}$ -biomass	$\delta^{15}\text{N}$ -p-NO ₃ ⁻	$\delta^{18}\text{O}$ -p-NO ₃ ⁻	HONO/NO _x	MCE
PIPO	2	19.9	-5.3	12.6	147.9	-1.1	0.3	-7.5	14.3	0.13	0.93
PIPO	3	35.8	1.7	11.6	124.7	2.3	0.3			0.29	0.94
PIPO	4	152.9	-3.1	10.6	716.8	-3.6	0.3			0.21	0.93
PICO	5	74.8	-2.3	8.8	170.8	-1.1	-3.4	-7.4	14.8	0.44	0.93
PICO	6	17.6	-1.9	8.4	94.7	1.4	-3.4			0.19	0.94
PIEN	8	25.7	-1.7	14.6	91.7	0.1	-2.4			0.28	0.92
PIEN	9	21.3	-4.8	9.5	73.6	-1.3	-2.8			0.29	0.93
PSME	10	42.2	-0.5	5.2	229.7	1.9	-1.4	-10.6	14.5	0.18	0.94
PSME	11	112.3	-0.4	15.2	571.8	3.3	-2.0			0.20	0.95
PIEN-d	12	17.1	-4.6	8.5	36.2	-4.3	-1.4	-9.9	11.5	0.47	0.87
PSME	14	25.3	0.1	14.9	70.0	2.1	-1.9			0.36	0.93
ABLA-c	15	51.0	2.1	9.9	95.5	3.4	-2.6	-8.9	12.7	0.53	0.89
PIPO-l	16	70.0	5.8	7.5	443.3	5.2	0.9			0.16	0.95
PIEN-c	17	47.1	6.1	14.8			-3.5				0.89
PSME-c	18	45.3	2.5	14.0			-1.4				0.93
PIPO-c	19	23.8	5.3	14.8	73.3	7.0	-0.1			0.32	0.93
PICO-c	20	52.5	3.0	14.9			-3.1				0.94
PICO-l	21	9.9	0.3	15.2			-4.2				0.93
PSME-l	22	40.0	1.9	10.2			-2.3				0.95
ABLA-c	23	40.8	0.5	12.2			-2.6				0.95

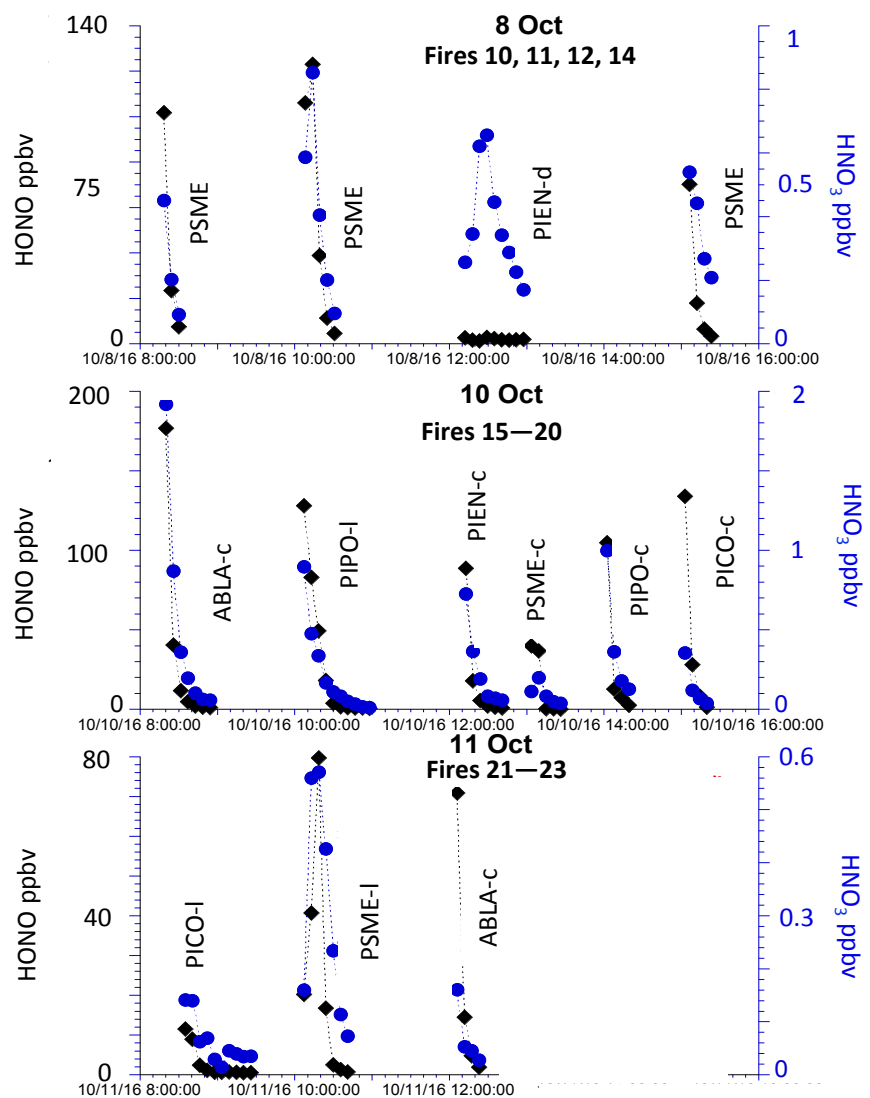


Figure 1. Temporal profile of HONO (black diamond) and HNO₃ (blue circle) concentration for various stack fires (fire numbers are referred to Table 1).

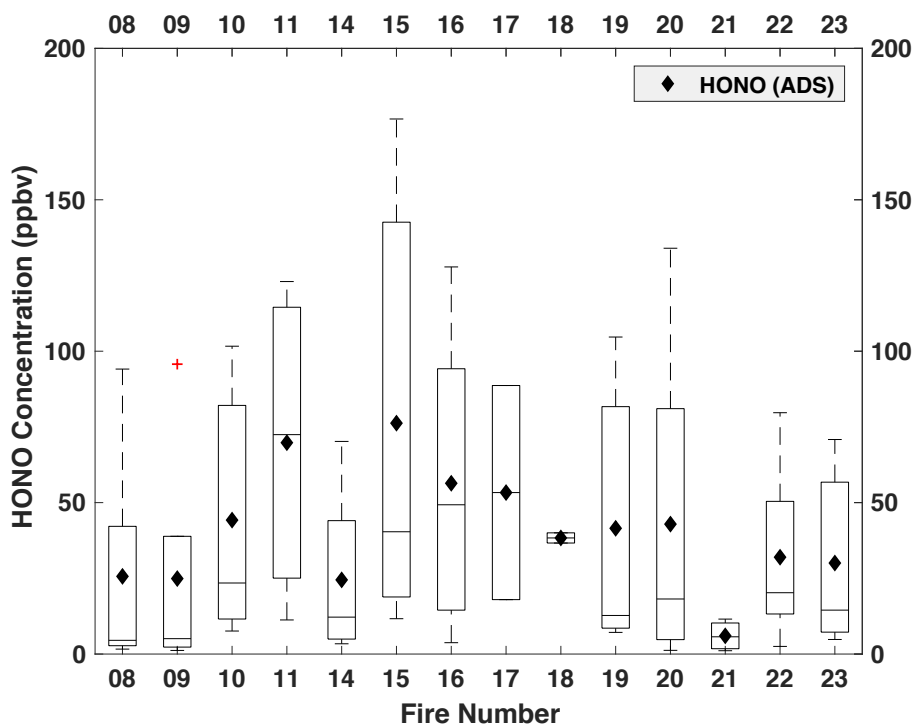


Figure 2. Box plot of MC/IC HONO measurement with 5 minutes resolution over the course of each fire. Each box whisker represents 5th, 25th, 50th, 75th, 95th percentile of HONO concentration during each collection period. Black diamond is the mean HONO concentration recovered from ADS collection. The red cross symbolize outliers.

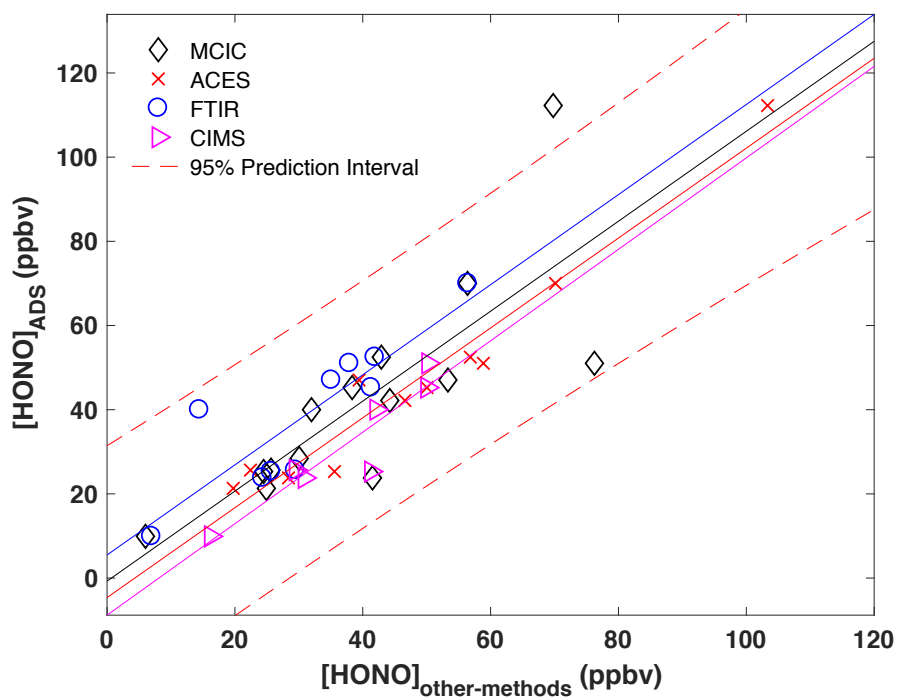


Figure 3. Comparison of ADS measured HONO concentration with mean values of various high resolution methods including MC/IC, FTIR, ACES and PTR-ToF for available fires. Solid lines are linear regression of each dataset with the same symbol color.

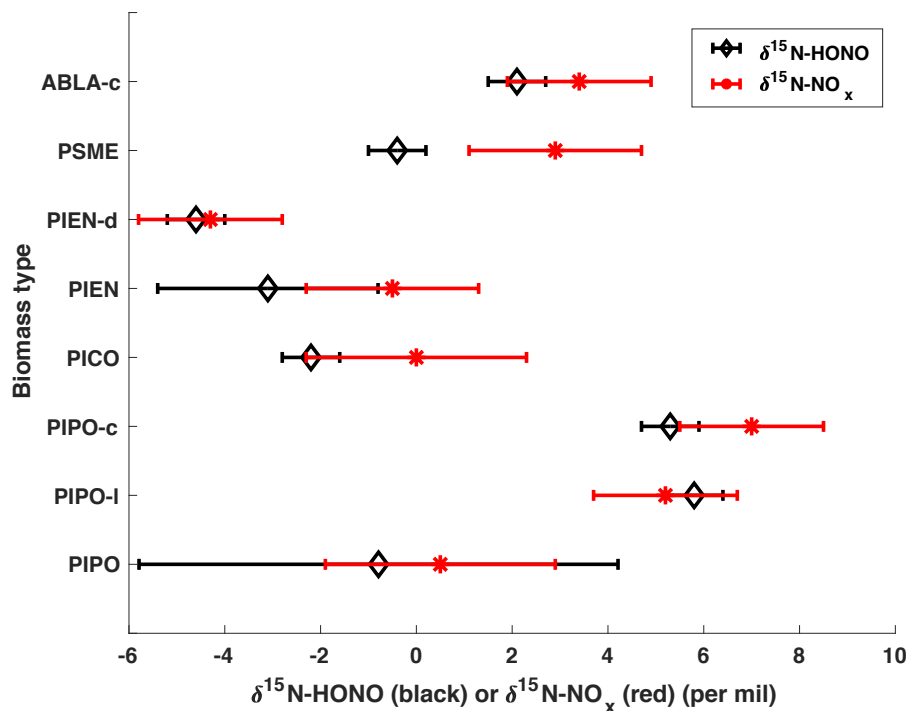


Figure 4. Concentration weighted mean $\delta^{15}\text{N}$ - of HONO and NO_x versus biomass type. The error bars are propagation of replicate $\pm 1\sigma$ uncertainty (when $n > 1$) and method uncertainty; otherwise, the error bars stand for method uncertainty. PIPO is ponderosa pine, PICO is lodgepole, PIEN is Engelmann spruce, PSME is Douglas-fir, ABLA is subalpine (from Fish Lake, canopy). l indicates litter, c indicates canopy, d indicates duff.

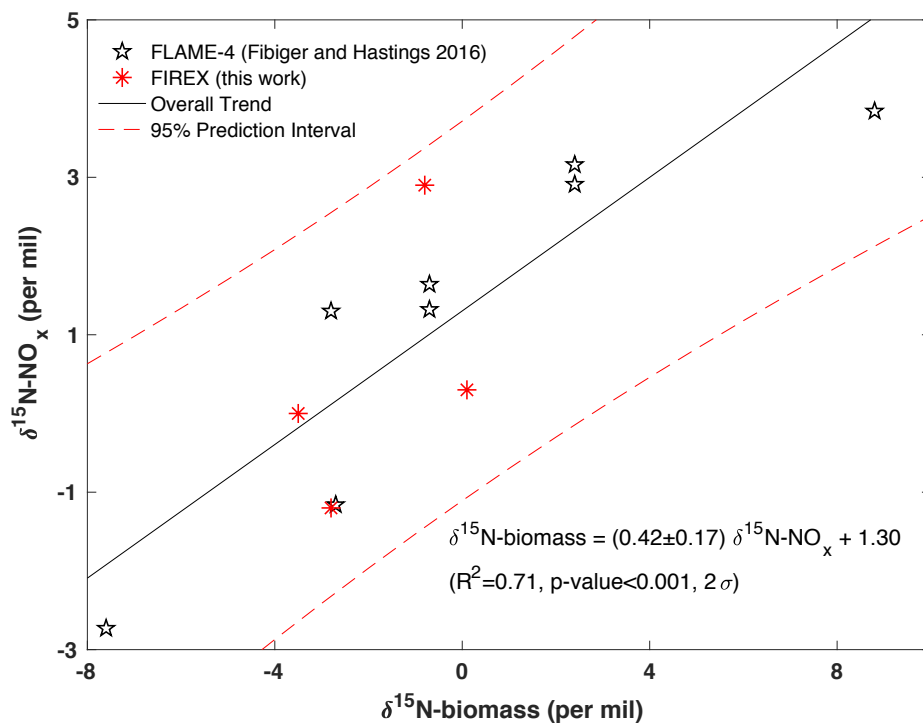


Figure 5. Dependence of $\delta^{15}\text{N-NO}_x$ on $\delta^{15}\text{N-biomass}$. Star data points represent results from FLAME-4 study (Fibiger and Hastings, 2016); Asterisk data points represent results from this work; solid line is linear regression between $\delta^{15}\text{N-NO}_x$ and $\delta^{15}\text{N-biomass}$ for the combined dataset; dashed lines are 95% prediction interval (2σ).

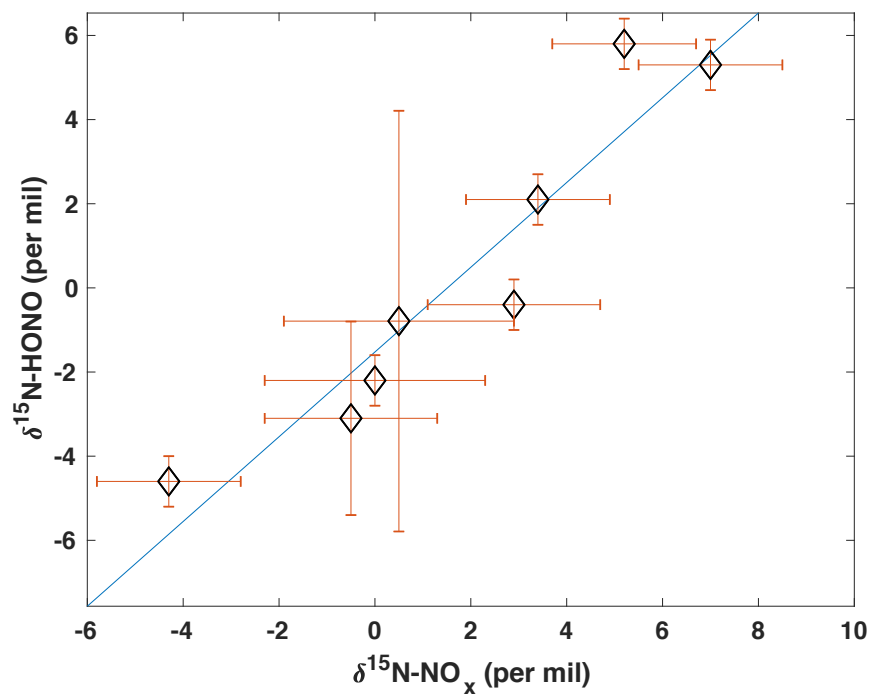


Figure 6. Scatter plot between $\delta^{15}\text{N-HONO}$ and $\delta^{15}\text{N-NO}_x$. All error bars are propagation of replicate uncertainty ($\pm 1\sigma$) and method uncertainty. Linear regression follows $\delta^{15}\text{N-HONO} = 1.01 \delta^{15}\text{N-NO}_x - 1.52$ ($R^2 = 0.89$, $p < 0.001$).